

2D Layered Perovskites

Solution Processable Materials

The recent discovery that single-layer 2D perovskites can be prepared using solution processing techniques¹ has been followed by enormous research into optoelectronic applications of 2D perovskites including light emitting diodes (LEDs),² phototransistors,³ and solar cells.⁴

Tunable Emission Wavelength

Photoluminescent 2D perovskites have an emission wavelength that changes depending on the layer thickness and the choice of amine and halide. We offer an excellent portfolio of the most popular 2D perovskite compositions for photoluminescence based devices.

Improved Moisture Stability

Solar cells fabricated with 2D perovskites have improved stability in moist air compared to 3D perovskites.⁴



Formula	Cat. No.	Layer Thickness	$(\text{RNH}_3)_2(\text{MeNH}_2)_{n-1}\text{Pb}_n\text{X}_{3n+1}$		
			R	X	n
$(\text{BA})_2\text{PbI}_4$	910961	n=1	Bu	I	1
$(\text{BA})_2\text{PbBr}_4$	910953	n=1	Bu	Br	1
$(\text{PEA})_2\text{PbI}_4$	910937	n=1	PE	I	1
$(\text{PEA})_2\text{PbBr}_4$	910945	n=1	PE	Br	1
$(\text{BA})_2(\text{MA})\text{Pb}_2\text{I}_7$	912816	n=2	Bu	I	2
$(\text{BA})_2(\text{MA})_2\text{Pb}_3\text{I}_{10}$	912557	n=3	Bu	I	3
$(\text{BA})_2(\text{MA})_3\text{Pb}_4\text{I}_{13}$	914363	n=4	Bu	I	4
$(\text{BA})_2(\text{MA})_4\text{Pb}_5\text{I}_{16}$	912301	n=5	Bu	I	5

BA = n-butylammonium; PEA = 2-phenylethylammonium; MA = methylammonium, Bu=n-butyl, PE=2-phenylethyl

References:

- 1) Dou, L.; Wong, A. B.; Yu, Y.; Lai, M.; Kornienko, N.; Eaton, S. W.; Fu, A.; Bischak, C. G.; Ma, J.; Ding, T.; Ginsberg, N. S.; Wang, L.-W.; Alivisatos, A. P.; Yang, P. *Science* **2015**, *349*, 1518. DOI: 10.1126/science.aac7660
- 2) Yuan, M.; Quan, L. N.; Comin, R.; Walters, G.; Sabatini, R.; Voznyy, O.; Hoogland, S.; Zhao, Y.; Beauregard, E. M.; Kanjanaboos, P.; Lu, Z.; Kim, D. H.; Sargent, E. H. *Nat. Nanotechnol.* **2016**, *11*, 872. DOI: 10.1038/NNANO.2016.110
- 3) Shao, Y.; Liu, Y.; Chen, X.; Chen, C.; Sarpkaya, I.; Chen, Z.; Fang, Y.; Kong, J.; Watanabe, K.; Taniguchi, T.; Taylor, A.; Huang, J.; Xia, F. *Nano Lett.* **2017**, *17*, 7330. DOI: 10.1021/acs.nanolett.7b02980
- 4) Cao, D. H.; Stoumpos, C. C.; Farha, O. K.; Hupp, J. T.; Kanatzidis, M. G. *J. Am. Chem. Soc.* **2015**, *137*, 7843. DOI: 10.1021/jacs.5b03796

SigmaAldrich.com/perovskite

The Life Science business of Merck operates as MilliporeSigma in the U.S. and Canada.

© 2022 Merck KGaA, Darmstadt, Germany and/or its affiliates. All Rights Reserved. Merck, the vibrant M, and Sigma-Aldrich are trademarks of Merck KGaA, Darmstadt, Germany or its affiliates. All other trademarks are the property of their respective owners. Detailed information on trademarks is available via publicly accessible resources.

MK_AD9822EN 43729 09/2022

The Life Science business of Merck operates as MilliporeSigma in the U.S. and Canada.

Sigma-Aldrich[®]
Lab & Production Materials

Sodiophilic Current Collectors Based on MOF-Derived Nanocomposites for Anode-Less Na-Metal Batteries

Huihua Li, Huang Zhang, Fanglin Wu, Maider Zarrabeitia, Dorin Geiger, Ute Kaiser, Alberto Varzi,* and Stefano Passerini*

“Anode-less” sodium metal batteries (SMBs) with high energy may become the next-generation batteries due to the abundant resources. However, their cycling performance is still insufficient for practical uses. Herein, a metal organic frameworks (MOF)-derived copper-carbon (Cu@C) composite is developed as a sodiophilic layer to improve the Coulombic efficiency (CE) and cycle life. The Cu particles can provide abundant nucleation sites to spatially guide Na deposition and the carbon framework offer void volume to avoid volume changes during the plating/stripping process. As a result, Cu@C-coated copper and aluminum foils (denoted as Cu-Cu@C and Al-Cu@C foil) can be used as efficient current collectors for sodium plating/stripping, achieving, nearly 1600 and 240 h operation upon cycling at 0.5 mA cm^{-2} and 1 mA h cm^{-2} , respectively. In situ dilatometry measurements demonstrate that Cu@C promotes the formation of dense Na deposits, thereby inhibiting side reactions, dendrite growth, and accumulation of dead Na. Such current collectors are employed in Na metal cells using carbon-coated $\text{Na}_3\text{V}_2(\text{PO}_4)_3$ (NVP/C) and copper selenides ($\text{Cu}_{2-x}\text{Se@C}$) cathodes, achieving outstanding rate capability and improved cycling performance. Most noticeably, “anode-less” Na batteries using Al-Cu@C as anode and NVP/C as cathode demonstrate promising CE as high as 99.5%, and long-term cycling life.


1. Introduction

Sodium (Na), the most abundant alkali metal in the Earth,^[1] has been considered a sustainable alternative charge carrier to lithium (Li) for high-performance, low-cost, and large-scale batteries.^[2] However, sodium-ion batteries (SIBs) still provide relatively low energy density compared to lithium-ion batteries.^[3] Therefore, the development of high energy electrode materials with long-term cycling stability is highly needed

for the practical application of SIBs. On the anode side, metallic sodium is the ideal candidate. In fact, with its high theoretical capacity (1166 mA h g^{-1}) and low redox potential (-2.71 V vs standard hydrogen electrode), sodium could enable high energy batteries. Indeed, multiple battery chemistries based on sodium metal anodes (SMAs) have been proposed, such as sodium-sulfur (commercial),^[4] sodium-air,^[5] sodium-seawater,^[6] and sodium-carbon dioxide batteries.^[7] However, similar to the Li-metal anode, metallic Na suffers from a few crucial problems, i.e., side reactions with the electrolyte and formation of Na dendrites, which may cause both cell failure and safety concerns.^[8] The commonly used ester-based electrolytes are particularly affected by side reactions with sodium.^[9] Comparatively, ether-based electrolytes feature improved stability, making them more suitable for reactive metal anodes.^[10] Besides the side reactions, the growth of dendritic Na upon repeated plating/stripping process

is another phenomenon leading to both performance deterioration and safety issues. On one side, Na dendrites, with their large surface area, are more reactive to the electrolyte causing more severe side reactions.^[11] Additionally, the cumulative growth of Na-metal dendrites, originating from the non-uniform charge distribution at the electrode–electrolyte interface, might penetrate the separator and lead to a short-circuit of the cell.^[8a] Finally, the uneven Na deposition results in the solid electrolyte interphase (SEI) of SMAs to repeatedly break

H. Li, H. Zhang, F. Wu, M. Zarrabeitia, A. Varzi, S. Passerini
Helmholtz Institute Ulm (HIU)
Helmholtzstrasse 11, D-89081 Ulm, Germany
E-mail: alberto.varzi@kit.edu; stefano.passerini@kit.edu

 The ORCID identification number(s) for the author(s) of this article can be found under <https://doi.org/10.1002/aenm.202202293>.

© 2022 The Authors. Advanced Energy Materials published by Wiley-VCH GmbH. This is an open access article under the terms of the Creative Commons Attribution License, which permits use, distribution and reproduction in any medium, provided the original work is properly cited.

H. Li, H. Zhang, F. Wu, M. Zarrabeitia, A. Varzi, S. Passerini
Karlsruhe Institute of Technology (KIT)
P.O. Box 3640, D-76021 Karlsruhe, Germany
D. Geiger, U. Kaiser
Central Facility for Electron Microscopy
Group of Electron Microscopy of Materials Science
Ulm University
Albert-Einstein-Allee 11, 89081 Ulm, Germany

DOI: 10.1002/aenm.202202293

and regenerate, leading to the formation of electrically inactive (“dead”) sodium. This results in low Coulombic efficiency (CE) and gradual consumption of the sodium anode.^[2b,12] Apart from such similarities, there are specific differences in nucleation and dendrite growth behavior between Li and Na metal, as listed in Table S1 (Supporting Information).

To tackle the aforementioned problems, various approaches have been developed, such as utilizing ester-based electrolytes to inhibit side reactions,^[10] employing electrolyte additives for efficient SEI growth,^[13] constructing artificial SEI layers on the sodium surface,^[9] and designing 3D current collectors.^[8b,14] Among all approaches, 3D current collectors with sodiophilic character can help to regulate the nucleation and growth of Na metal deposits, which can result on improved efficiency and integrity of the negative electrode.^[15] In fact, 3D current collectors with a large surface area can limit the volume change during sodium deposition and dissolution, as well as decrease the effective current density to inhibit the formation of dendrites.^[8b] Moreover, a sodiophilic interface can promote Na nucleation, thus allowing for more uniform electrodeposition.^[16] For example, a carbon cloth decorated with SnO₂ quantum dots was reported to efficiently improve the electrochemical deposition of Na.^[15] With a similar strategy, Li et al. constructed a 3D network with sodiophilic polyacrylonitrile fiber film as a scaffold for uniform Na deposition.^[17] Despite these earlier works, a novel and simple strategy to construct a 3D current collector with sodiophilic property on conventional copper and aluminum current collectors is highly desired. Wu et al. applied C@Sb nanoparticles with core-shell structure on a copper current collector. Such nucleation buffer layer enabled uniform deposition of Na metal for an extended number of cycles.^[16] This rational design of nanostructured composite nucleation agent opens up a promising avenue to achieve reversible Na-metal deposition.

Despite the appealing properties of Na, the manufacturing/assembly of batteries with a metallic Na anode is not practical, given its high reactivity. In this respect, “anode-less” (or “anode-free”) cells promise high safety and low-cost high-energy density sodium metal batteries (SMBs).^[18] However, given the limited sodium inventory supplied by the cathode,^[19] enabling a highly efficient Na deposition/dissolution on the anode current collector is essential to achieve high performance cells.

In this work, we demonstrate a facile strategy to construct a robust nucleation buffer layer by applying a Cu-based MOF (Cu-BTC) -derived composite, i.e., copper nanoparticles embedded in carbon framework (denoted as Cu@C), on conventional current collectors. The Cu@C composites enable low nucleation barriers for sodium deposition on both copper and aluminum current collectors, which can be attributed to the abundant nucleation sites guiding Na deposition. The large surface area and porosity of the carbon-based layer also provides empty volume to minimize the overall volume changes upon Na plating/stripping. These characteristics enable higher CE and lower voltage hysteresis upon Na plating/stripping when using Cu@C modified Cu/Al collectors compared to the bare Cu/Al foils. More importantly, we demonstrated that the Cu@C nucleation layer can help to obtain a dense (i.e., dendrite-free) and uniform Na deposition

layer by in situ electrochemical dilatometry. As a result, SMBs using pre-sodiated (5 mA h cm⁻²) Cu-Cu@C or Al-Cu@C foils as negative electrode (anode) and Na₃V₂(PO₄)₃/C as positive electrode (cathode) deliver excellent rate performance and cycling stability. Ultimately, “anode-less” SMBs were also fabricated employing Cu-Cu@C and Al-Cu@C current collectors, which exhibited a promising (although still improvable) cycling stability over 80 and 30 cycles with an average CE up to 99.1% and 99.5%, respectively.

2. Results and Discussion

2.1. Material Synthesis and Characterization

The Cu-BTC precursors were synthesized as reported in our previous work.^[20] The final Cu@C composites were then obtained via a simple pyrolysis method as described in the experimental part. As shown in **Figure 1a**, the X-ray diffraction (XRD) pattern of the as-prepared Cu@C composites evidences the presence of metallic Cu (JCPDS 04–0836). No obvious carbon-related diffraction peak could be detected, probably due to the small size of the graphitic domains. The nature of the carbon component in Cu@C was therefore investigated by Raman spectroscopy (Figure S1, Supporting Information). Two characteristic peaks located at 1362 and 1592 cm⁻¹ were observed, which can be assigned to the bands of disordered sp³-type (D-band) and graphitic sp²-type (G-band) carbon, respectively.^[21] Noticeably, the intensity of the G-band is higher than D-band, indicating a relatively high content of graphitic (sp²-hybridized) carbon, which could be attributed to a catalytic effect of the Cu nanoparticles promoting carbon graphitization during the carbonization process.^[22] X-ray photoelectron spectroscopic (XPS) experiments were carried out to confirm the surface chemical composition of the Cu@C composites (Figure S1b–d, Supporting Information). The detailed C 1s spectrum (Figure S1b, Supporting Information) is dominated by the peaks at 284.40 and 285.04 eV, which are related to the graphitic sp²-C and carbon sp³-C, respectively. Further peaks at 286.36, and 288.74 correspond to the –CO–(ethers), and –COOR (esters) groups, respectively.^[23] The high-resolution Cu 2p_{3/2} spectrum is displayed in Figure S1c (Supporting Information). The main peak located at 932.02 eV is ascribed to Cu⁺ in Cu₂O.^[24] The low intensity peaks toward higher binding energies (the first peak at 933.84 eV followed by four peaks at 1.37, 7.41, 8.54, and 10.59 eV binding energy higher), which includes the satellite peaks between 944.43–941.25 eV, can be ascribed to Cu²⁺ as CuO.^[24] The O 1s region (Figure S1d, Supporting Information) confirmed the species observed in C 1s and Cu 2p_{3/2}, exhibiting Cu₂O at 530.21 eV and CuO at 531.06 eV,^[25] suggesting the presence of oxides on the surface of the Cu@C composite. In addition, the content of copper in Cu@C was calculated from thermogravimetric analysis (TGA) measurements in O₂ atmosphere (Figure S2, Supporting Information). Assuming that all Cu in Cu@C is transformed into CuO during the heating process under O₂ atmosphere; its content in the composite accounts to 68 wt.% (the detailed calculations can be found in the Supporting Information). Also, the specific surface area and pore size distribution of Cu@C were evaluated via

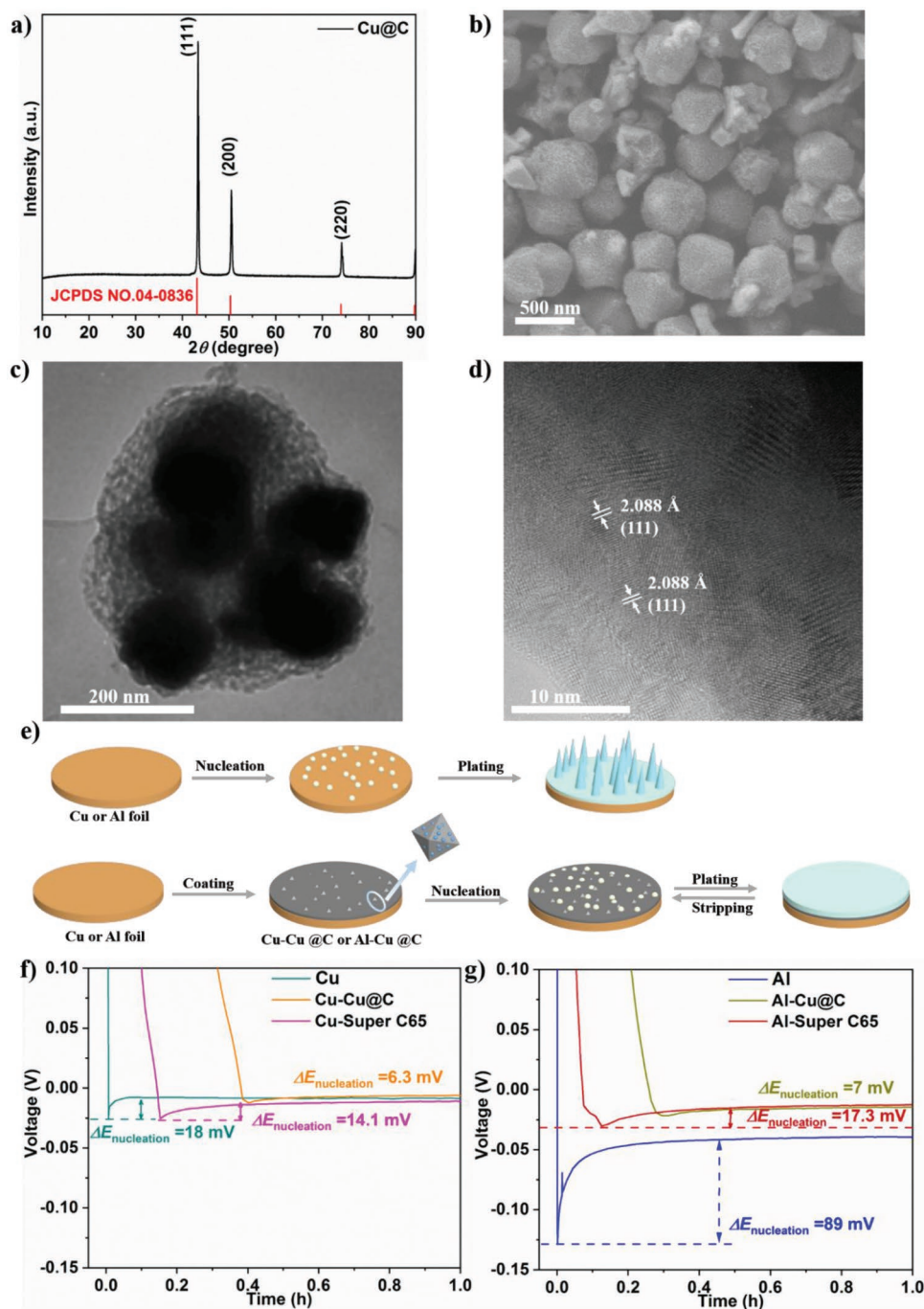


Figure 1. a) XRD pattern and b) SEM of Cu@C. c,d) High-resolution TEM (HR-TEM) images of Cu@C with different magnifications. e) Schematics of Na deposition on bare Cu or Al foils and Cu-Cu@C or Al-Cu@C. f) Comparison of the sodium nucleation overpotential in Na|Cu, Na|Cu-Cu@C, and Na|Cu-Super C65 cells. g) Comparison of the sodium nucleation overpotential in Na|Al, Na|Al-Cu@C, and Na|Al-Super C65 cells. (At 1 mA cm⁻² with 1 M NaPF₆ in diglyme at 20 °C)

N₂ adsorption–desorption experiment. As shown in Figure S3 (Supporting Information), the Cu@C demonstrates a specific Brunauer–Emmett–Teller (BET) surface area of 139 m² g⁻¹ with an average pore size of 2 nm, which can provide sufficient contact area with the electrolyte and facilitate the ionic transport. The morphology of Cu-BTC and Cu@C composites was studied by scanning electron microscopy (SEM) and transmission

electron microscopy (TEM). The overall morphology of the precursor is well maintained after carbonization (Figure 1b; Figure S4, Supporting Information)). However, the surface of the composite becomes rough and uneven, due to the growth of metal (or metal oxides) particles and the decomposition of the organic ligands. The microstructure of Cu@C was further investigated by TEM. As shown in Figure 1c,d, the Cu

nanoparticles are embedded in the carbon matrix. The high-resolution TEM image in Figure 1d shows the lattice fringes of the (111) plane with a d spacing of 2.1 Å. The energy dispersion X-ray spectroscopy (EDX) elemental mapping of Cu@C (Figure S5, Supporting Information) indicates that Cu and C atoms are homogeneously distributed in the composites.

The process of fabricating the modified current collectors and electrochemical Na deposition are elucidated in Figure 1e. On the bare Cu or Al foil current collector, the Na⁺ flux will be preferably concentrated on rough spots to nucleate (Figure S6a,b, Supporting Information), leading to the uneven Na-metal deposition and ultimately resulting in Na-metal dendrite growth.^[14] However, it is expected that using Cu@C-coated Cu or Al foil as current collector, the uniform Na deposition may be guided by the composite layer. Besides, the 3D carbon framework can not only increase the specific surface area to enhance electrolyte contact but also provide empty space to accommodate Na metal, thus limiting the overall volumetric change of the anode during Na plating/stripping. To investigate the role of the nucleation buffer layer, sodium plating experiments were performed at 1 mA cm⁻², using bare Cu (or Al), Cu-Super C65 (or Al-Super C65), and Cu-Cu@C (or Al-Cu@C). The nucleation overpotential upon galvanostatic plating is defined as the difference between the bottom of the voltage dip and the flat voltage plateau.^[26] Figure 1f,g demonstrates that the initial Na nucleation overpotential of bare Cu (Al), Cu-Super C65 (Al-Super C65), and Cu-Cu@C (Al-Cu@C) are 18 (89), 14.1 (17.3), and 6.3 (7) mV, respectively. These results clearly illustrate that the incorporation of Cu@C composites effectively decreases the nucleation barrier for Na plating on both Cu and Al current collectors, suggesting the improved sodiophilic property.^[27]

2.2. Electrochemical Behavior of Bare Cu and Cu-Cu@C Current Collectors

To evaluate the morphological evolutions upon Na deposition, coin cells were assembled using bare Cu or Cu-Cu@C current collectors as working electrodes and Na metal as counter electrodes, and Na was plated at 1 mA cm⁻². Figure S6 (Supporting Information) shows the SEM images of pristine Cu and Cu-Cu@C foils. As it can be seen, no obvious defects or cracks can be observed in the bare Cu foil, while some particles with a size smaller than 1 μm are spread on the surface, which may cause inhomogeneous current distribution promoting dendrite growth.^[28] Differently, the Cu-Cu@C displays a porous structure constituted by the Cu@C composite layer (Figure S6c,d, Supporting Information). Upon plating, 1 (stage I), 3 (stage II), and 6 mA h cm⁻² (stage III) of Na on the bare Cu foil, uneven Na deposition with evident cracks is observed in Figure 2 and Figure S7 (Supporting Information). The inset of Figure 2d shows the optical image of the electrode after deposition of Na (6 mA h cm⁻²) on the bare Cu foil, reflecting the inhomogeneous plating caused by the high nucleation barrier.^[29] In contrast, Na is homogeneously deposited on the Cu-Cu@C. After plating 1 and 3 mA h cm⁻², the porous structure of Cu@C can still be identified, indicating the capability of such a composite layer to host sodium metal and avoid large volume change upon deposition. Increasing the capacity to 6 mA h cm⁻², the smooth

and flat Na deposition is still occurring, enabled by the composite layer. The corresponding picture also demonstrates the smooth and shiny Na metal layer deposited on the Cu-Cu@C foil (the inset of Figure 2g).

To evaluate the Na plating/stripping reversibility, cells were assembled with bare Cu or Cu-Cu@C foil as the working electrode and Na metal as the counter and reference electrode, which were cycled at different current densities and capacities. For the plating/stripping tests, all the cells were initially activated at 0.1 mA cm⁻² for ten full cycles between 0.01 and 1 V to form a stable SEI and compensate the sodium loss. The cell employing Cu-Cu@C displays the highest CEs during the ten initial activation cycles (Figure S8a, Supporting Information). As shown in Figure S8b (Supporting Information), the Cu-Cu@C current collector exhibits stable and high CE with an average value of 99.9% for nearly 400 cycles (≈1600 h) at 0.5 mA cm⁻² and 1 mA h cm⁻². In contrast, the bare Cu current collector showed a rather scattered CE indicative of soft short circuits due to Na dendritic growth. An ex situ SEM image recorded on the bare Cu electrode and separator after Na|Cu cell failure (Figure S8c) clearly demonstrates that Na dendrites grow on the bare Cu and through the separator. When increasing the current density to 1 mA cm⁻², sodium can still be efficiently plated/stripped onto the Cu-Cu@C foil for over 600 cycles (≈1200 h) with an average CE of 99.8%. On the other hand, the CE of bare Cu foil was very scattered (Figure 2 h) and the cell failed after about 100 cycles. It is worth noting that the voltage hysteresis for the cell using Cu-Cu@C is in the range of 17–26 mV (see inset of Figure 2 h), i.e., substantially smaller than that of the cell employing bare Cu foil (34–55 mV). This demonstrates the superior kinetics of the Cu-Cu@C current collector. Furthermore, at a current density of 3 mA cm⁻² and a plated capacity of 3 mA h cm⁻² (Figure S8d, Supporting Information), the cell with Cu-Cu@C foil still displays stable CE with an average value of 99.9% for nearly 180 cycles (360 h), further demonstrating the potential of this approach to enable practical high-energy rechargeable SMBs.

To better understand the role of the Cu@C layer on the Na plating/stripping behavior, in situ electrochemical dilatometry was employed. Note that fresh cells without activation were used for the dilatometry, resulting on lower initial CE compared to the previous measurements (Figure 2). Figure 3 displays the electrode thickness variation (magenta line) of bare Cu (Figure 3a) and Cu-Cu@C (Figure 3b) electrodes during the first three galvanostatic Na plating/stripping cycles (voltage profiles are also shown in cyan). Upon the first cycle, the thickness change curves display three distinct regions/regimes. As seen, the thickness of bare Cu was almost unchanged in region 1 (time: ≈15 min, capacity: 0.125 mA h cm⁻²). We can confidently assume that here only SEI formation occurs. A rapid thickness increase is observed then in region 2 when the electrode potential drops below 0 V and metallic sodium begins being deposited on the Cu surface. At the end of the plating step, the total thickness change of 15.5 μm for bare Cu was measured. Actually, the theoretical electrode thickness change (h_{theo}) upon Na plating can be calculated from the Equation (1):^[30]

$$h_{\text{theo}} (\mu\text{m}) = \frac{3.6 \times 10^4 \times Q \times M_{\text{Na}}}{F \times \rho_{\text{Na}}} = 10 \mu\text{m} \quad (1)$$

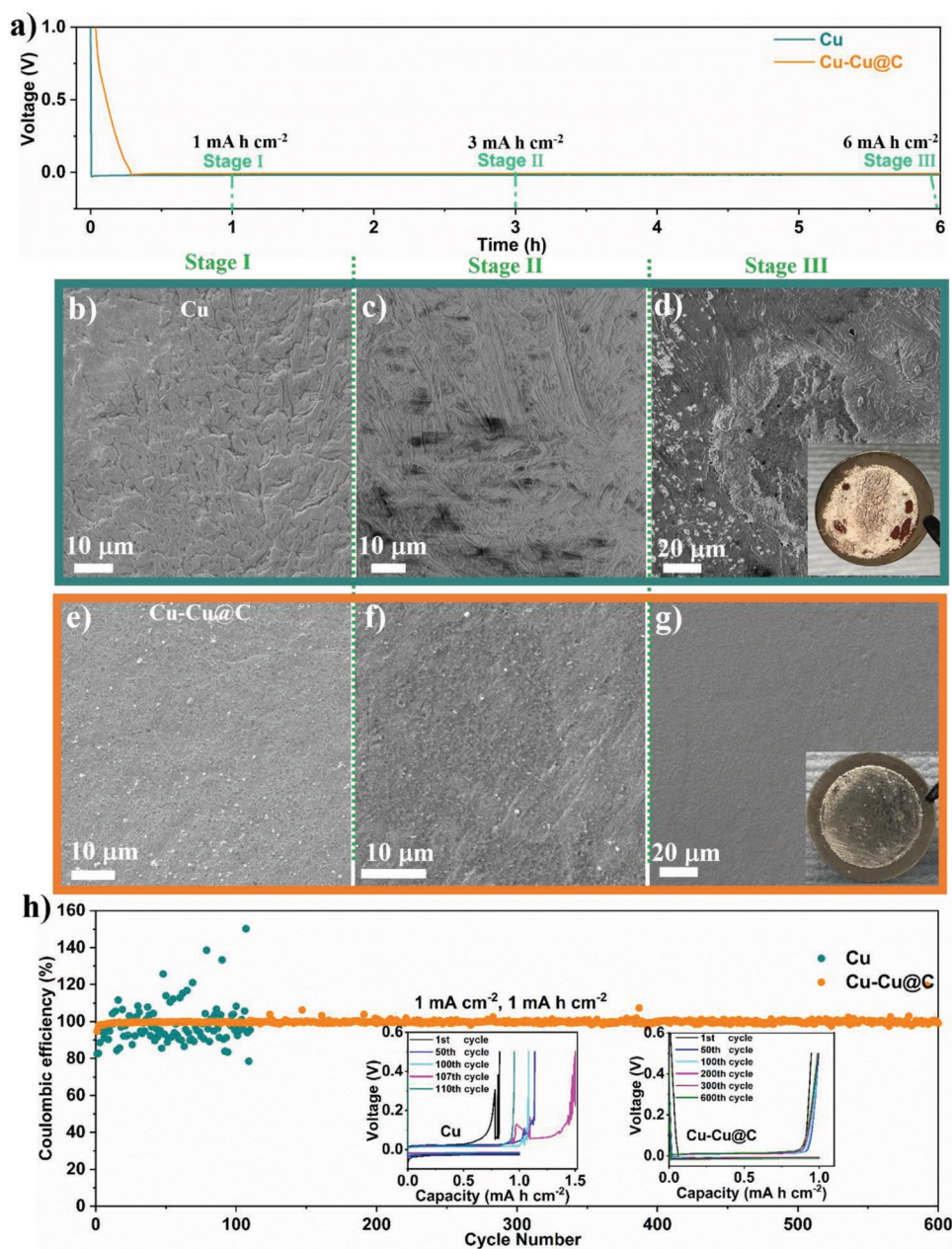


Figure 2. a) Voltage profiles of Na|Cu and Na|Cu-Cu@C cells upon galvanostatic Na plating. SEM images of b–d) bare Cu and e–g) Cu-Cu@C current collectors along Na plating of 1 (stage I), 3 (stage II) and 6 mA h cm⁻² (stage III). The insets show the photographs of bare Cu and Cu-Cu@C foil current collectors after 6 mA h cm⁻² Na plating. h) Comparison of the Na plating/stripping CE at 1 mA cm⁻² and 1 mA h cm⁻² for bare Cu and the Cu-Cu@C current collectors in Na|Cu and Na|Cu-Cu@C cells. The insets show selected voltage profiles upon galvanostatic Na plating/stripping on bare Cu and Cu-Cu@C at 1 mA cm⁻². (All the cells employed 1 m NaPF₆ in diglyme as electrolyte and were tested at 20 °C)

where Q is the areal Na plating charge (1 mA h cm⁻²), M_{Na} is the Na molar mass (23 g mol⁻¹), F is the Faraday constant (96485 A s mol⁻¹) and ρ_{Na} is the sodium density (0.862 g cm⁻³). The measured thickness change of 15.5 μm is substantially larger than what theoretical expected (10 μm). Meanwhile, the porosity (P) of the Na deposition on bare Cu is estimated to be ≈33% according to the formula (2):

$$P(\%) = \left(1 - \frac{h_{\text{theo}}}{h_{\text{measured}}}\right) \times 100 \quad (2)$$

These results suggest that a porous (dendritic) Na film was formed on the Cu current collector during the first Na plating. After that, the thickness decreases when stripping Na from the Cu surface (region 3). However, the reversible thickness change is only 4.1 μm, leading to an irreversible thickness expansion of 11.4 μm. Additionally, as shown in Figure 3a and Figure S9a (Supporting Information), the irreversible thickness change continues in the following cycles, leading to the accumulation of ≈10 μm after ten cycles (corresponding to a mean rate of ≈1 μm per cycle). According to literature, the

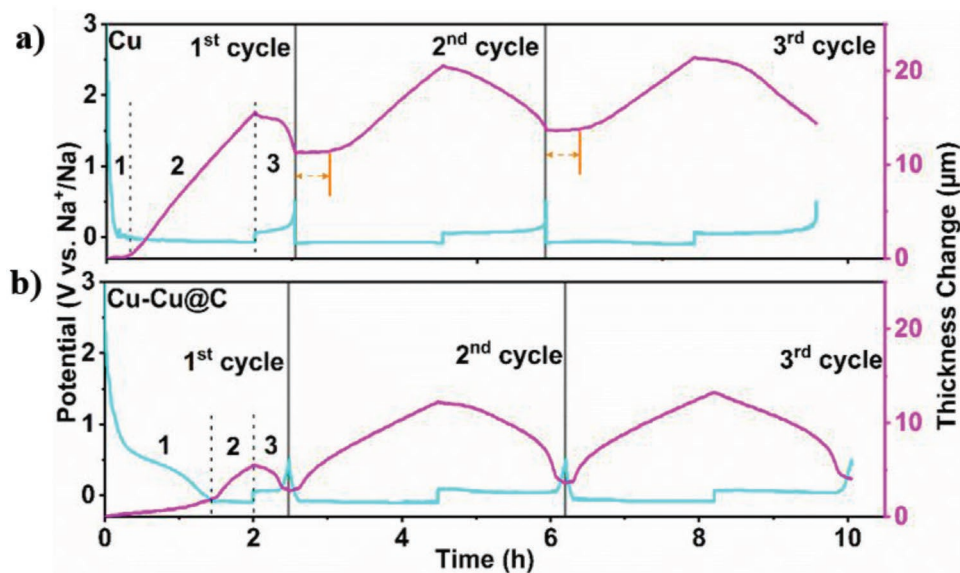


Figure 3. In situ dilatometry investigation of bare Cu and Cu-Cu@C at a current density of 0.5 mA cm^{-2} and with a Na plating charge fixed at 1 mA h cm^{-2} : voltage profile and corresponding thickness change of a) bare Cu and b) Cu-Cu@C during the first three cycles.

SEI layer has usually a thickness ranging from a few to several hundreds of nanometres.^[30–31] Therefore, the irreversible thickness expansion must mainly originate from the accumulation of dead Na. Additionally, and most interestingly, the thickness change profile upon the subsequent cycles also present a similarly unchanged region during the initial plating of Na (time: $\approx 28 \text{ min}$, capacity: $0.23 \text{ mA h cm}^{-2}$), which could be attributed to the reformation of SEI. The repeated reformation of SEI layer upon cycling not only consumes electrolyte and fresh Na, but also causes the uncontrolled Na dendrites formation.^[8b] Overall, this would lead to low CE, rapid capacity fading, and inferior cycling life of SMBs using bare Cu.

In contrast, the Cu-Cu@C slightly expands in the initial sloping region 1, probably as result of sodium insertion into the carbon matrix of the Cu@C layer, as well as SEI formation. Afterward, the thickness rapidly increases upon plating of Na on the Cu-Cu@C surface. However, the overall thickness change of Cu-Cu@C electrode during the first sodiation step is only $4.5 \mu\text{m}$, simply because a large portion of the capacity (limited to 1 mA cm^{-2}) is employed for SEI formation and storage of Na in the carbon matrix, therefore less Na metal is deposited. Nevertheless, this formation step is crucial. In fact, from the second cycle onwards, a thickness change of $\approx 10 \mu\text{m}$ was always measured (Figure 3b; Figure S9b, Supporting Information), which is practically the same as the theoretical value. This suggests that a relatively dense (i.e., dendrite-free) and uniform Na layer is electrodeposited on/in the Cu-Cu@C. Furthermore, the thickness contraction also approaches $\approx 10 \mu\text{m}$, which demonstrates an excellent thickness reversibility higher than 99.9% and probably negligible accumulation of dead Na. Overall, we can confidently conclude that the Cu@C layer allows for the formation of an efficient SEI during the first sodiation, which inhibits detrimental reactions such as continuous electrolyte consumption and accumulation of dead Na, thus resulting on more homogeneous and dense Na deposition compared to a bare Cu foil.

2.3. Electrochemical Behavior of Bare Al and Al-Cu@C Current Collectors

In order to really enable a cost efficient sodium battery technology, Al is a more suitable choice for the current collectors ($\$0.3$ and $\$1.2 \text{ m}^{-2}$ for Al and Cu foils, respectively).^[32] In this context, the above approach was applied to investigate the Na deposition on bare Al and Al-Cu@C foils. The SEM images of the pristine Al foil and Al-Cu@C foil electrodes are shown in Figure S10 (Supporting Information). The overall deposition behaviour on the bare Al and Al-Cu@C foil is rather similar to that observed for the Cu-based current collectors. Al-Cu@C exhibited a very homogeneous Na deposition behavior. As seen in Figure S11 (Supporting Information), the Cu@C buffer layer still retains the original structure after plating 0.25 , 0.5 , and $0.75 \text{ mA h cm}^{-2}$ Na metal, indicating that Cu@C is a very effective substrate for Na deposition. As seen in Figure 4e,f and Figure S12d,e (Supporting Information), the Cu@C buffer layer still retains the original structure after plating 1 and 3 mA h cm^{-2} Na metal (stage I and II in Figure 4a). When the sodium loading is increased to 6 mA h cm^{-2} (stage III in Figure 4a), the SEM images (Figure 4g; Figure S12f, Supporting Information) and photograph (inset of Figure 4g) clearly reveal the smooth surface of the Na-metal deposited on the Cu@C composite layer, proving that it acts as a robust nucleation layer for Al foil. Instead, a cracked and inhomogeneous layer is formed on the bare Al foil after deposition of increasingly higher amounts of Na (Figure 4b–d; Figure S12a–c, Supporting Information). Figure 4h exhibits the CEs of bare Al and Al-Cu@C electrodes cycled at 0.5 mA cm^{-2} and 1 mA h cm^{-2} . Unstable CE values are observed for the bare Al foil in the initial cycles, while the Cu@C modified Al foil displayed much longer cycle life up to 60 cycles (240 h) with a high average CE of $\approx 97.5\%$ indicating the improved Na deposition behavior also at higher current density, i.e., 1.0 mA cm^{-2} and 1 mA h cm^{-2} (Figure 4i). Also, the voltage profiles in Figure S13

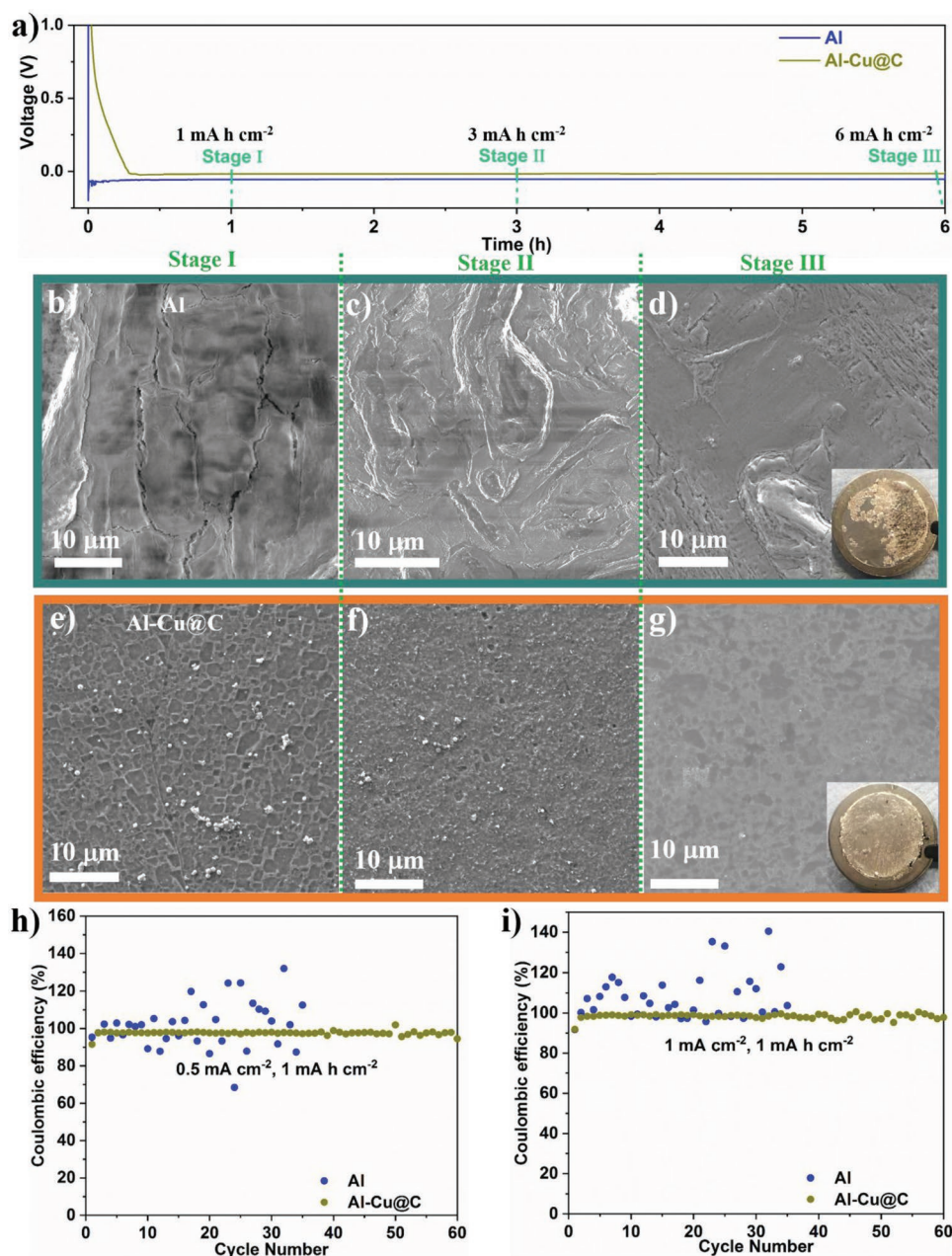


Figure 4. Electrode morphology evolution upon Na deposition. a) Voltage profiles upon galvanostatic (1 mA cm^{-2}) deposition of Na in Na|Al and Na|Al-Cu@C cells. SEM images of b–d) bare Al and e–g) Al-Cu@C current collectors along Na plating of 1 (stage I), 3 (stage II) and 6 mA h cm^{-2} (stage III). The insets show the photographs of bare Al and Al-Cu@C foil current collectors after 6 mA h cm^{-2} Na plating. Comparison of the Na plating/stripping CE of bare Al and the Al-Cu@C electrode at h) 0.5 mA cm^{-2} (1 mA h cm^{-2}) capacity and i) 1 mA cm^{-2} (1 mA h cm^{-2}) capacity, respectively. (All the cells employed 1 M NaPF_6 in diglyme as electrolyte and were tested at 20°C)

(Supporting Information) show that the steep CE oscillation for bare Al foil employing cell delivers much inferior cycling stability. This clearly demonstrates that Na dendrite growth is effectively suppressed by the Cu@C layer.

In addition, the surface chemistry of the formed SEI on bare Al and Cu@C modified Al was analysed after 10 cycles plating/stripping (Figure S14, Supporting Information). NaPF_6 covers the surface of bare Al foil because the sample was not washed to avoid any reactions of Na metal with the washing solvent

(see F 1s in Figure S14a). After partially removing the NaPF_6 salt, the bare Al foil shows Al metal and Al_2O_3 from the current collector (Al 2P Figure S14a). Meanwhile, the Cu@C modified Al does not show Al or Cu signal. The fact that Al is only observed on bare Al foil suggests that the formed SEI, in this case, is thinner and/or less homogeneous than in Cu@C modified Al. Although different SEI thickness and/or homogeneity is observed, the SEI composition in both samples is similar, but with varying concentration of species. The SEI formed on bare

Al foil contains more sodium- and fluorine-based species (i.e., Na_xPF_y , $\text{Na}_x\text{PO}_y\text{F}_z$ and NaF) than the SEI on Cu@C modified Al, indicating that NaPF_6 decomposes at a larger extent in the first case.^[33] However, similar concentrations of carbon-oxygen species are observed, such as hydrocarbon (-C-C-/-C-H-), ethers (-C-O-), carbonyl group compounds (-C=O) and ester (-COOR), due to the diglyme reduction reactions.^[34] The fact that the Cu@C modified Al foil shows higher Na concentration than bare Al (Figure S14b), but lower sodium- and fluorine-based and sodium- and carbon-based species suggests the presence of higher concentration of Na metal, which is in agreement with the SEM images.

The galvanostatic cycling performance of the Na|Na symmetric cells was tested to evaluate the cycling stability and the overpotential of Na pre-loaded electrodes (5 mA h cm^{-2}) denoted as Cu (5 Na), Cu-Cu@C (5 Na), Al (5 Na) and Al-Cu@C (5 Na). A detailed description is provided in the Supporting Information (Figures S15 and S16, Supporting Information).

To further investigate the Al-Cu@C foil in practical cells, Na metal cells consisting of NVP/C and pre-sodiated Al-Cu@C (5 Na) or Al (5 Na) electrodes were assembled and tested under galvanostatic cycling conditions in the 2.5–3.8 V voltage range. As shown in Figure 5a; Figure S17a, Supporting Information), the Al-Cu@C (5 Na)|NVP/C cell stood for 1300 cycles with a reversible capacity of $\approx 87 \text{ mA h g}^{-1}$ and an average CE of 99.9% at 5C ($1\text{C} = 120 \text{ mA g}^{-1}$). However, the cell employing Al (5 Na) anode failed after only 66 cycles clearly due to the dendritic Na growth (see the last charge–discharge profile in Figure S17b, Supporting Information) leading to short circuit.^[35] The SEM images of the anodes after cycling at 5C were also collected (Figure S17c,d, Supporting Information). The surface of the Al (5 Na) anode was rather uneven and rough, due to the growth of sodium dendrites. In contrast, the Al-Cu@C (5 Na) electrode showed a very flat and smooth surface after 1300 cycles, indicating that the composite Cu@C layer warrants the stable operation of the sodium metal cell.

Besides NVP/C, carbon-coated Cu_{2-x}Se was also employed as cathode for assembling sodium metal cells (denoted as Al (5 Na)| $\text{Cu}_{2-x}\text{Se}@C$ and Al-Cu@C (5 Na)| $\text{Cu}_{2-x}\text{Se}@C$). As seen in Figure 5 and Figure S18 (Supporting Information), the Al-Cu@C (5 Na)| $\text{Cu}_{2-x}\text{Se}@C$ cell displays better rate performance than Al (5 Na)| $\text{Cu}_{2-x}\text{Se}@C$, showing discharge capacities of 270, 266, 261, 256, 249, 235, and 209 mA h g^{-1} at 0.1, 0.2, 0.5, 1, 2, 5, and 10 A g^{-1} , respectively. Lowering the rate to the lowest value, the capacity recovered to 266 mA h g^{-1} . Moreover, after the C-rate test, the cell showed excellent cycle life, performing 420 cycles at 2 A g^{-1} without obvious capacity loss (Figure 5b). Long-term cycling tests at 2 A g^{-1} were also performed on fresh Al (5 Na)| $\text{Cu}_{2-x}\text{Se}@C$ and Al-Cu@C (5 Na)| $\text{Cu}_{2-x}\text{Se}@C$ cell (Figure 5c; Figure S18c, Supporting Information). The latter cell did not show capacity decay over 700 cycles, while the Al (5 Na)| $\text{Cu}_{2-x}\text{Se}@C$ achieved only 65 cycles before short-circuiting (Figure S18d, Supporting Information). These results confirm once again that the sodiophilic Cu@C nanocomposite suppresses the formation of Na dendrites and enables the use of cost-effective Al as current collector in SMBs. To evaluate the applicability of Cu-Cu@C foil in conventional SMBs, full-cells were also assembled and investigated. A detailed description is

provided in the Supporting Information (Figures S19–S21, Supporting Information).

2.4. “Anode-less” Sodium-Metal Full-Cells

“Anode-less” SMBs are very attractive, due to the avoided use of Na metal, they promise low manufacturing cost and safety, as well as increased specific energy. Herein, “anode-less” sodium metal cells were assembled through using the Cu-Cu@C or Al-Cu@C foil as the negative electrode and NVP/C as the positive electrode.

Initially, full-cell with limited sodium excess were assembled using pre-deposited (2 mA h cm^{-2}) Al-Cu@C electrodes (denoted as Al-Cu@C (2 Na)). The Al-Cu@C (2 Na)|NVP/C full-cell exhibited a stable cycling life for 400 cycles with a reversible capacity of about 96 mA h g^{-1} (based on the cathode active material mass) and an average CE of 99.6% (Figure 6a). The overall cell discharge–charge profiles as well as the individual contributions from the cathode and the anode are shown in Figure 6b and Figure S22b,c (Supporting Information), respectively, demonstrating the reversibility of sodium metal anode.

Finally, “anode-less” cells with no sodium excess cell were also developed using bare Al and Al-Cu@C current collectors. To minimize the initial irreversible capacity, the Al and Al-Cu@C current collectors were pre-activated. Specifically, a plating step at 1 mA cm^{-2} with capacity limited to 2 mA h cm^{-2} was performed. This was then followed by a stripping step up to 0.02 V versus Na/Na^+ . Such activation procedure enabled efficient SEI formation, while entirely removing the deposited metallic Na from the current collector (see Figure 6c). However, it should be mentioned that in the case of Al-Cu@C the carbonaceous network of the Cu@C composite may also host Na ions to a certain extent. These cannot be extracted from the carbon matrix at such cut-off voltage (i.e., 0.02 V), therefore we cannot exclude a small Na reservoir being present in the activated electrode. Figure 6d displays the initial charge–discharge profiles of the “anode-less” cell using the Al-Cu@C current collector at 1C ($1\text{C} = 120 \text{ mA g}^{-1}$), which clearly demonstrate the full utilization of the positive electrode active material. The initial discharge capacity of the “anode-less” cell can reach 102 mA h g^{-1} based on the cathode mass (i.e., areal capacity of $0.33 \text{ mA h cm}^{-2}$, Figure 6e). The cycling performance at 1C is shown in Figure 6e,f and Figure S23a,b (Supporting Information). An obvious capacity fading is, however, observed after 30 cycles. On the other hand, the “anode-less” cell using bare Al foil could barely be charged once (Figure S23c, Supporting Information).

The capacity fading of the Al-Cu@C|NVP/C full-cell appears related with the high (average 99.5%), but still not acceptable CE. In fact, the discharge profiles of the cell show a voltage decay (see Figure 6f) caused by the increasing anode potential upon discharge, suggesting that Na is still irreversibly consumed upon cycling. An “anode-less” cell using the Cu-Cu@C electrode was also fabricated, showing promising cycling performance at 1C over 80 cycles with CE steady at 99.1% (Figure S24, Supporting Information, see the related text in Supporting Information for a detailed discussion). To better identify the promise of such systems, the specific gravimetric energy was

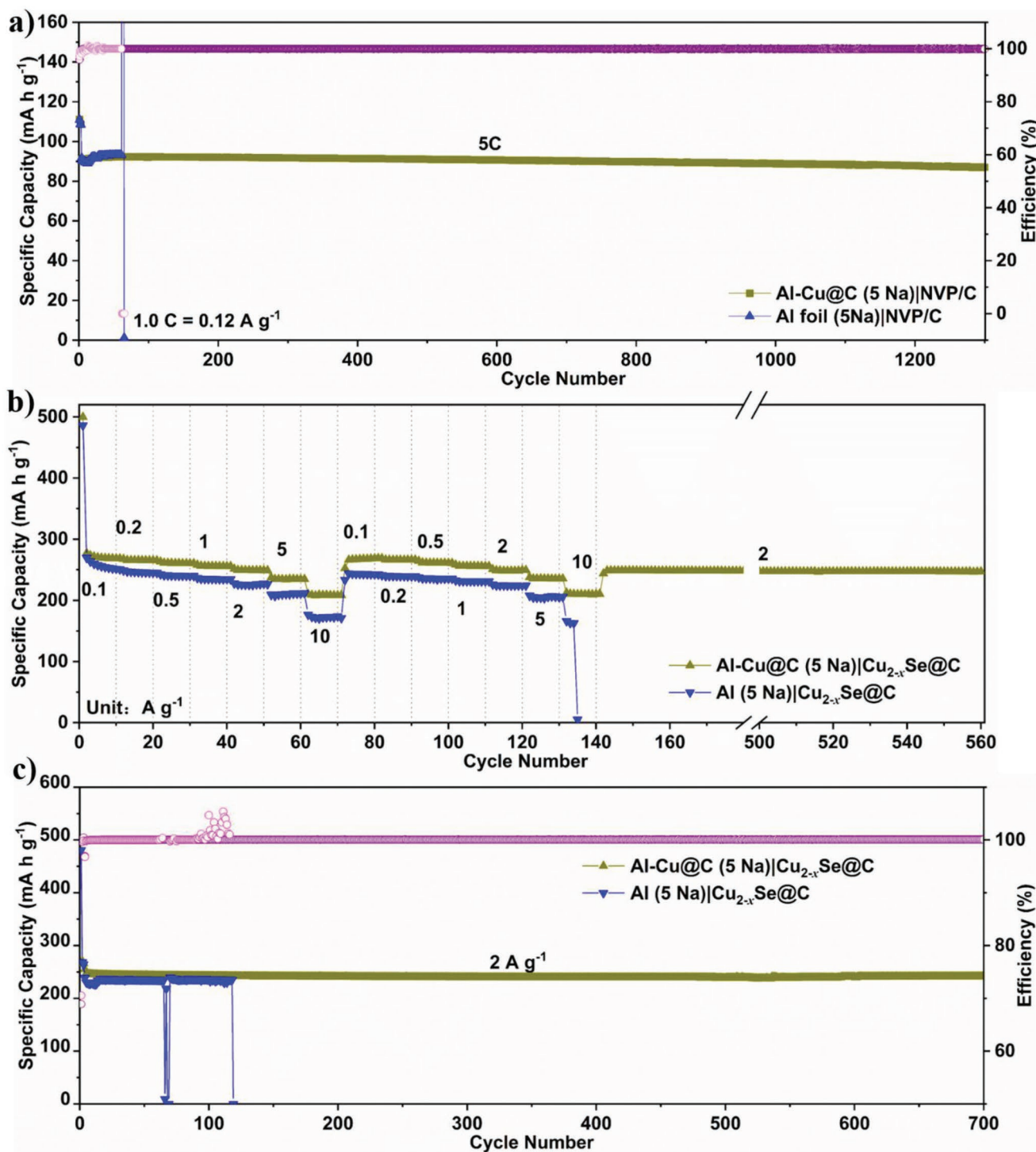


Figure 5. a) Comparison of Al-Cu@C (5 Na)|NVP/C and Al (5 Na)|NVP/C cells' cycling performance at 5C (1C = 120 mA g⁻¹). Comparison of Al (5 Na)|Cu_{2-x}Se@C and Al-Cu@C (5 Na)|Cu_{2-x}Se@C cells b) rate and c) long term cycling (at 2 A g⁻¹) performance. (All the cells employed 1 m NaPF₆ in diglyme as electrolyte and were tested at 20 °C)

calculated from the discharge voltage profiles. A maximum value of ≈ 248 and 236 Wh kg^{-1} can be obtained at 1C for Cu-Cu@C|NVP/C and Al-Cu@C|NVP/C, respectively, based on the active electrode materials, i.e., including the cathode and the

coating layer on anode current collector, but not including the masses of binder, Super C65, and current collector. It should be noted that this cycling performance of Cu-Cu@C|NVP/C and Al-Cu@C|NVP/C is comparable and even superior to previous

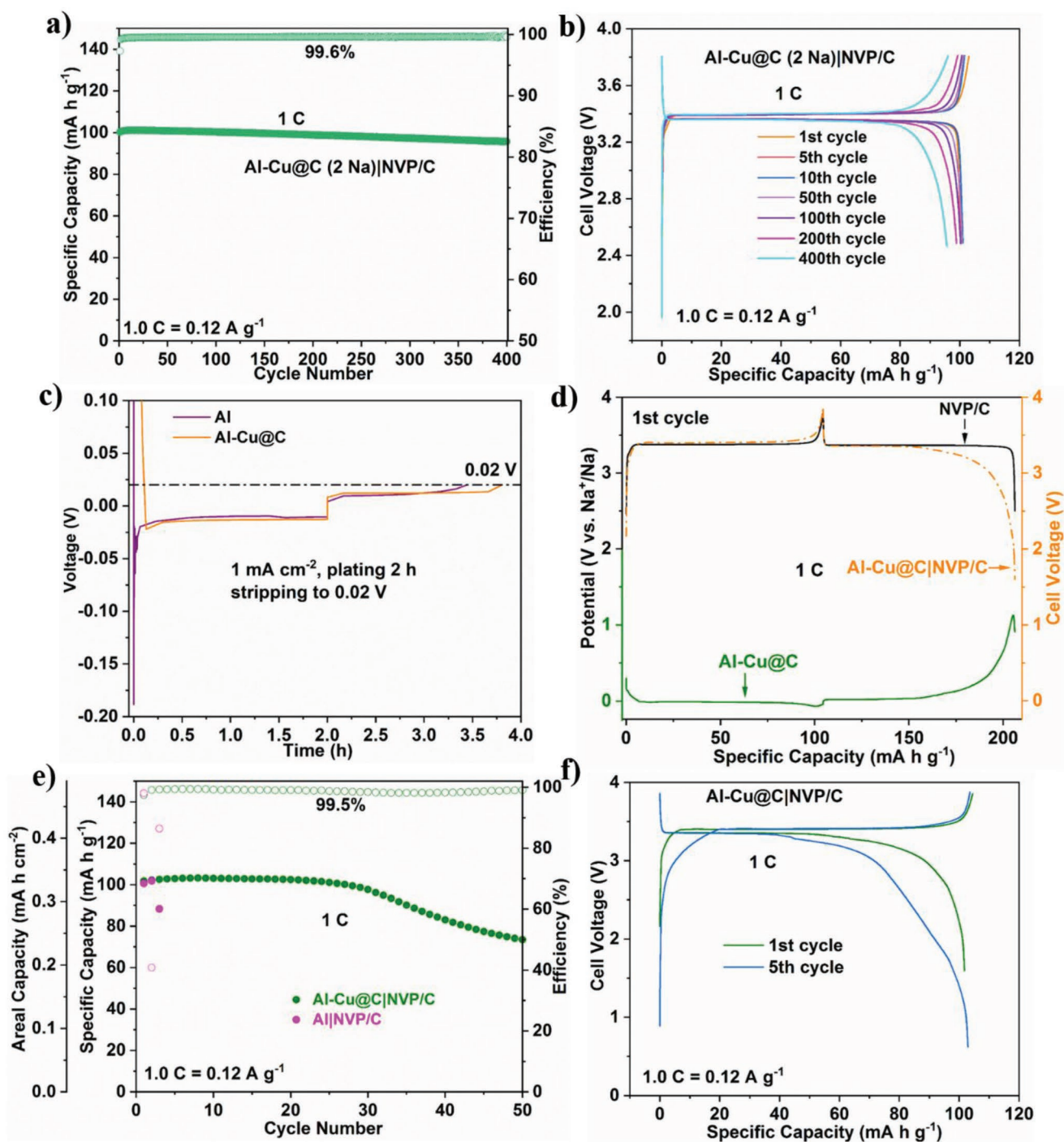


Figure 6. a) Cycling performance and b) selected discharge–charge profiles (1st, 5th, 10th, 50th, 100th, 200th, and 400th cycle) of Al-Cu@C (2 Na)|NVP/C full-cell at 1C. c) The activation process of Al-Cu@C and bare Al foil at 1.0 mA cm⁻². d) The first cycle discharge–charge profile at 1C for the “anode-less” full-cell (orange dashed/dotted line) and NVP/C cathode (black solid line) as well as Al-Cu@C foil anode (green solid line). e) Cycling performance at 1C of Al-Cu@C|NVP/C and Al|NVP/C “anode-less” full-cells. f) Selected dis-/charge profiles of Al-Cu@C|NVP/C “anode-less” full cell (1st and 5th). (All the cells employed 1 M NaPF₆ in diglyme as electrolyte and were tested at 20 °C)

iron sulfides reported in the literature (see list in Table S2, Supporting Information). Nevertheless, the same type of fading mechanism was observed for the Al-Cu@C|NVP/C and Cu-Cu@C|NVP/C full-cells indicating that further optimization is needed “anode-less” SMBs. While enhanced electrolyte

formulations may allow for increased cycling stability and improved rate capability, the developed “anode-less” cells give encouraging prospects with regards to the implementation of high energy SMBs, especially in terms of suppressed Na dendrite growth.

3. Conclusion

In summary, a novel metal organic frameworks-derived Cu@C composite developed as a sodiophilic layer for sodium metal anodes. Depositing such a composite layer on commercial Cu or Al current collector foils, results in achieving low Na nucleation overpotential, outstanding Coulombic efficiency upon cycling, and low voltage hysteresis as demonstrated in both asymmetric and symmetric cells for sodium metal stripping/plating. In situ dilatometry measurements indicated that the Cu@C nucleation layer favours the formation of dense Na deposits and suppresses thickness increase due to accumulation of dead Na, resulting in the good cycling stability upon Na plating/stripping. Taking advantage of the improved current collectors, sodium metal cells using NVP/C and Cu_{2-x}Se@C cathodes exhibit outstanding rate performance and cycling stability. The Al-Cu@C (5 Na)|NVP/C full-cell delivers a high reversible capacity of 87 mA h g⁻¹ for 1300 cycles with an average CE of 99.9%. Most importantly, Na dendrite growth is clearly suppressed. Moreover, even “anode-less”, i.e., zero excess, SMBs operating for a few tens of cycles can be made using Cu@C-coated anodic current collectors, which show CEs higher than 99%. Even though further improvements are necessary, the reported results demonstrate that a proper engineering of commercial Cu or Al foils can enable “anode-less” sodium metal batteries.

4. Experimental Section

Chemicals: Copper nitrate trihydrate (Cu(NO₃)₂·3H₂O, 98.0-103%) and Selenium powder (Se, ≥99.5%) were obtained from Sigma-Aldrich and Alfa Aesar, respectively. 1,3,5-benzenetricarboxylic acid (BTC, 98%) was purchased from Acros Organics. Methanol (98.5%) and Polyvinylpyrrolidone (PVP, K30, Mw = 44000-54000) were obtained from VWR and PanReac AppliChem, respectively. All the chemicals were used as received without further purification.

Synthesis of Cu-BTC Precursors and Derivatives: The synthesis of Cu-BTC precursors followed the previous work.^[20,36] Typically, 0.9 g Cu(NO₃)₂·3H₂O and 0.4 g polyvinylpyrrolidone (PVP, K-30) were completely dissolved into 50 mL methanol at room temperature under vigorous stirring. Following, 0.43 g 1,3,5-benzenetricarboxylic acid (BTC), also dissolved in 50 mL methanol at room temperature under vigorous stirring, were slowly injected into the former solution. Then, the mixture was aged at room temperature for 24 h. The precipitate was collected via centrifugation and washed with methanol for several times. Finally, the powders were dried at 80 °C overnight to obtain the precursors (Cu-BTC). To obtain the derivatives, the Cu-BTC precursors were carbonized at 500 °C for 2 h in a tube furnace at a rate of 2 °C min⁻¹ under Ar flow. After cooling down to room temperature, the Cu@C powders were obtained.

Synthesis of Carbon-coated Na₃V₂(PO₄)₃ Composite cathode: The carbon-coated Na₃V₂(PO₄)₃ (NVP/C) composite was synthesized according to previous literature.^[37] Typically, CH₃COONa·3H₂O (VWR, ≥99%), NH₄VO₃ (Sigma-Aldrich, ≥99%), NH₄H₂PO₄ (Alfa Aesar, ≥99%), and citric acid monohydrate (C₆H₈O₇·H₂O) (Alfa Aesar, ≥99%) were dissolved into deionized water and dried at 80 °C. After being ground, the resulting powder was put in a tube furnace, pre-heated at 350 °C for 6 h and annealed at 800 °C for 12 h Argon flow. After natural cooling to room temperature, the NVP/C composite was collected.

Synthesis of Carbon-coated Cu_{2-x}Se (Cu_{2-x}Se@C) Composite Materials: The composites were obtained by a one-step selenidation process. Cu-BTC and selenium powders in a mass ratio of 1:5 were put downstream and upstream, respectively, in the same crucible in a tube

furnace. The tube furnace was heated at a rate of 2 °C min⁻¹ up to 500 °C and kept for 2 h under Ar flow. After cooling down to ambient temperature, the Cu_{2-x}Se@C composites were collected.

Materials Characterization: The crystal structure of Cu@C was determined via X-ray Diffractometry (XRD) using a Bruker D8 Advance instrument employing Cu K_α source (λ = 0.154 nm). TGA was performed under oxygen atmosphere with a heating rate of 5 °C min⁻¹ (TGA-209F, Netzsch). The pore size distribution and specific surface area of all samples were derived from the nitrogen absorption-desorption isotherms (Autosorb-iQ, Quantachrome) at 77 K. The morphological characteristics and elemental compositions were determined via Scanning Electron Microscopy (SEM, ZEISS 1550VP) coupled with an energy dispersion X-ray spectroscopy (EDX, Oxford). High-resolution Transmission Electron Microscopy (HRTEM, Titan 80–330 kV) was employed to investigate the crystal structure of the material. The Raman spectra of the sample were measured on a confocal InVia Raman microspectrometer (He-Ne laser of 633 nm, Renishaw). X-ray Photoelectron Spectroscopy (XPS) measurement of Cu@C was performed in an ultrahigh vacuum analysis chamber (10⁻¹⁰ mbar) using the monochromatic Al K_α (1486.6 eV) X-ray radiation and the Phoibos 150 XPS spectrometer (SPECS-Surface concept) equipped with a microchannel plate and a delay line detector in fixed transition mode. The peak fitting was analyzed by CasaXPS software. Adventitious carbon (C–C/C–H) peak at 285 eV was used as calibration.

Electrochemical Measurements: The plating/stripping tests were performed in half-cell (coin cell) configuration directly using Na metal as the counter electrode and the pristine/modified current collectors as the working electrode. The Cu@C coated current collectors were prepared by casting a slurry mixture of the active materials (Cu@C), Super C65 (Imerys Graphite & Carbon), and polyvinylidene fluoride (PVDF, Solef 6020, Solvay) in N-methyl pyrrolidone (NMP, anhydrous, Sigma-Aldrich) with a mass ratio of 70:20:10 on Al or a dendritic copper foil (Schlenk, 99.9%) foils. The Super C65-decorated current collectors were obtained by casting a slurry of Super C65 and PVDF (weight ratio 9:1) in NMP on Cu or Al foils. The diameter of the working electrodes and Na were 12 and 10 mm, respectively. The areal loading of the functional materials on the current collectors was ≈1.3–1.5 mg cm⁻² and the thickness of the casted film on the Al or Cu foil was ≈15 μm. Symmetric cells were assembled by using pre-deposited (5 mA h cm⁻² Na) bare Cu, bare Al, Cu-Cu@C or Al-Cu@C foils. Polypropylene discs (Celgard 2400) were used as separators and 1.0 M NaPF₆ in diglyme was selected as electrolyte for half-cells and symmetric cells (45 μL). For the plating/stripping tests, all the cells were initially activated at 0.1 mA cm⁻² for ten full cycles between 0.01 and 1 V to form a stable SEI. Subsequently, plating steps at current density of 0.5, 1 and 3 mA cm⁻² for 2, 1, and 1 h, respectively, were applied. In the following stripping steps, the cells were limited to a cut-off voltage of 0.5 V. The CE was calculated based on the ratio between the plating and stripping capacity.

To assemble conventional Na-metal cells, NVP/C cathodes were fabricated by coating a slurry composed of 80 wt.% NVP/C, 10 wt.% Super C65, and 10 wt.% PVDF in NMP onto Al current collector. The active material areal loading was ≈3.5–4.0 mg cm⁻². The Cu_{2-x}Se@C cathode were made by casting a slurry composed of Cu_{2-x}Se@C, Super C65, and PVDF (70:20:10 weight ratio) in NMP onto Cu foil (areal loading: 1.2–1.5 mg cm⁻²). Before cell assembly, all cathodes diameter: 12 mm) were pressed at 5 tons cm⁻² for 10 s to improve contact and increase their density. A glass fiber disc (Whatman, GF/D) was used as the separator and 1.0 M NaPF₆ in diglyme was used as electrolyte for the full-cells. Na pre-deposited (2 or 5 mA h cm⁻²) bare Cu, bare Al, Cu-Cu@C or Al-Cu@C foils were used as anode.

To assemble “anode-less” cells, the bare Cu, bare Al, Cu-Cu@C, or Al-Cu@C current collectors were subjected to an initial activation cycle (plating at 1 mA cm⁻² for 2 h down to 0.01 V, stripping up to 0.02 V) to form a stable SEI. Subsequently, “anode-less” sodium metal batteries were assembled using the pre-activated current collectors coupled with NVP/C cathodes within the voltage range of 2.5–3.8 V (the cathode potential was controlled). All the cells were assembled in an argon-filled glovebox (MBraun) with H₂O and O₂ content lower than 0.1 ppm.

In situ electrochemical dilatometry measurements upon galvanostatic Na plating/stripping on bare Cu and Cu-Cu@C were carried out using an ECD-3 Nano Dilatometer cell (from EL-CELL GmbH). In the dilatometry cell, the thickness of the working electrode (diameter: 10 mm) was 18 μm for bare Cu and 33 μm for Cu-Cu@C. Sodium metal foils served as counter electrode (diameter: 12 mm) and reference electrode, and a specific glass T-frit was used as separator soaked with ≈ 1.5 mL of the same electrolyte used for all other experiments. Measurements were conducted in a climatic chamber (Binder KB 23, Germany) at a constant temperature of 20 $^{\circ}\text{C}$. For the baseline stabilization, the cells were allowed to rest for 24 h while the open circuit voltage (OCV) was monitored. Galvanostatic Na plating/stripping tests were performed using an SP-150 potentiostat (Bio-logic Science Instruments), applying a constant current density of 0.5 mA cm^{-2} . The thickness variation of the working electrode was recorded using an E-852 controller box (PISeCa Signal Conditioner) and the EC-Lab software.

Supporting Information

Supporting Information is available from the Wiley Online Library or from the author.

Acknowledgements

The authors thank Seyed Milad Hosseini for the Raman measurement. The authors thank Xilai Xue for the dilatometry measurement. The authors also thank Dr. Zhen Chen for valuable discussions. H.L. gratefully acknowledges financial support from the Chinese Scholarship Council (CSC). Financial support from the Helmholtz Association and the German Ministry for Education and Research (BMBF, within the M.Era-net project "NEILLSBAT," 03XP0120A) is also acknowledged.

Open access funding enabled and organized by Projekt DEAL.

Conflict of Interest

The authors declare no conflict of interest.

Authors Contribution

H.L. conceived the research idea, designed the experiments, analyzed the results, and prepared the first draft of the manuscript. H.Z. provided some research ideas and cathode materials. F.W. provided some research ideas and valuable discussions. M.Z. contributed to the characterization by XPS. A.V. and S.P. supervised, coordinated the work, and provided funding. All authors contributed to the writing and have given approval to the final version of the manuscript.

Data Availability Statement

The data that support the findings of this study are available from the corresponding author upon reasonable request.

Keywords

anode-less batteries, dendrite-free formation, MOFs, nucleation layers, sodium metal batteries

Received: July 7, 2022
Revised: August 22, 2022
Published online:

- [1] J. K. Hwang, R. Hagiwara, H. Shinokubo, J. Y. Shin, *Mater. Adv.* **2021**, *2*, 2263.
- [2] a) M. D. Slater, D. H. Kim, E. Lee, C. S. Johnson, *Adv. Funct. Mater.* **2013**, *23*, 947; b) B. Y. Lee, E. Paek, D. Mitlin, S. W. Lee, *Chem. Rev.* **2019**, *119*, 5416; c) C. L. Zhao, Y. X. Lu, J. M. Yue, D. Pan, Y. R. Qi, Y. S. Hu, L. Q. Chen, *J. Energy Chem.* **2018**, *27*, 1584.
- [3] H. Kim, J. Y. Hong, K. Y. Park, H. Kim, S. W. Kim, K. Kang, *Chem. Rev.* **2014**, *114*, 11788.
- [4] H. Zhang, T. Diemant, B. S. Qin, H. H. Li, R. J. Behm, S. Passerini, *Energies* **2020**, *13*, 836.
- [5] a) Y. Kang, F. M. Su, Q. K. Zhang, F. Liang, K. R. Adair, K. F. Chen, D. F. Xue, K. Hayashi, S. C. Cao, H. Yadegari, X. L. Sun, *ACS Appl. Mater. Interfaces* **2018**, *10*, 23748; b) F. Liang, X. C. Qiu, Q. K. Zhang, Y. Kang, A. Koo, K. Hayashi, K. F. Chen, D. F. Xue, K. N. Hui, H. Yadegari, X. L. Sun, *Nano Energy* **2018**, *49*, 574.
- [6] Y. Kim, A. Varzi, A. Mariani, G. T. Kim, Y. Kim, S. Passerini, *Adv. Energy Mater.* **2021**, *11*, 2102061.
- [7] a) K. Pichaimuthu, A. Jena, H. Chang, C. C. Su, S. F. Hu, R. S. Liu, *ACS Appl. Mater. Interfaces* **2022**, *14*, 5834; b) X. F. Hu, P. H. Joo, E. Matios, C. L. Wang, J. M. Luo, K. S. Yang, W. Y. Li, *Nano Lett.* **2020**, *20*, 3620.
- [8] a) L. Zhang, X. D. Zhu, G. Y. Wang, G. Xu, M. H. Wu, H. K. Liu, S. X. Dou, C. Wu, *Small* **2021**, *17*, e2007578; b) Z. P. Li, K. J. Zhu, P. Liu, L. F. Jiao, *Adv. Energy Mater.* **2021**, 2100359; c) J. Yu, K. Shi, S. W. Zhang, D. F. Zhang, L. K. Chen, S. Li, J. B. Ma, H. Y. Xia, Y. B. He, *Sci. China Mater.* **2021**, *64*, 2409.
- [9] S. Y. Wang, Y. L. Jie, Z. H. Sun, W. B. Cai, Y. W. Chen, F. Y. Huang, Y. Liu, X. P. Li, R. Q. Du, R. G. Cao, G. Q. Zhang, S. H. Jiao, *ACS Appl. Energy Mater.* **2020**, *3*, 8688.
- [10] J. Zhang, D. W. Wang, W. Lv, L. Qin, S. Z. Niu, S. W. Zhang, T. F. Cao, F. Y. Kang, Q. H. Yang, *Adv. Energy Mater.* **2018**, *8*, 1801361.
- [11] C. Z. Luo, T. Shen, H. Q. Ji, D. Huang, J. Liu, B. Y. Ke, Y. H. Wu, Y. Chen, C. L. Yan, T. S. Chengzhao Luo, H. Ji, D. Huang, J. Liu, B. Ke, Y. Wu, Y. Chen, C. Yan, *Small* **2020**, *16*, e1906208.
- [12] Y. Zhao, K. R. Adair, X. L. Sun, *Energy Environ. Sci.* **2018**, *11*, 2673.
- [13] a) W. Fang, H. Jiang, Y. Zheng, H. Zheng, X. Liang, Y. Sun, C. H. Chen, H. F. Xiang, *J. Power Sources* **2020**, *455*, 227956; b) H. Wang, C. L. Wang, E. Matios, J. M. Luo, X. Lu, Y. W. Zhang, X. F. Hu, W. Y. Li, *Energy Stor. Mater.* **2020**, *32*, 244.
- [14] Y. Y. Lu, Q. Zhang, M. Han, J. Chen, *Chem. Commun. (Camb)* **2017**, *53*, 12910.
- [15] Y. Xu, E. Matios, J. M. Luo, T. Li, X. Lu, S. H. Jiang, Q. Yue, W. Y. Li, Y. J. Kang, *Nano Lett.* **2020**, *21*, 816.
- [16] G. Y. Wang, Y. Zhang, B. K. Guo, L. Tang, G. Xu, Y. J. Zhang, M. H. Wu, H. K. Liu, S. X. Dou, C. Wu, *Nano Lett.* **2020**, *20*, 4464.
- [17] Y. Xu, C. L. Wang, E. Matios, J. M. Luo, X. F. F. Hu, Q. Yue, Y. J. Kang, W. Y. Li, *Adv. Energy Mater.* **2020**, *10*, 2002308.
- [18] Y. X. Wang, H. Dong, N. Katyal, H. C. Hao, P. C. Liu, H. Celio, G. Henkelman, J. Watt, D. Mitlin, *Adv. Mater.* **2022**, *34*, 2106005.
- [19] H. Wang, Y. Wu, S. H. Liu, Y. Jiang, D. Shen, T. X. Kang, Z. Q. Tong, D. Wu, X. J. Li, C. S. Lee, *Small Methods* **2021**, *5*, 2001050.
- [20] H. H. Li, H. Zhang, T. Diemant, R. J. Behm, D. Geiger, U. Kaiser, A. Varzi, S. Passerini, *Small Struct.* **2021**, *2*, 2100035.
- [21] H. H. Li, Y. Ma, H. Zhang, T. Diemant, R. J. Behm, A. Varzi, S. Passerini, *Small Methods* **2020**, *4*, 2000637.
- [22] a) H. Xu, L. Zhao, X. Liu, Q. Huang, Y. Wang, C. Hou, Y. Hou, J. Wang, F. Dang, J. Zhang, *Adv. Funct. Mater.* **2020**, *30*, 2006188; b) S. Qiu, W. Xing, X. Feng, B. Yu, X. Mu, R. K. K. Yuen, Y. Hu, *Chem. Eng. J.* **2017**, *309*, 802.
- [23] Y. Ma, Y. J. Ma, G. T. Kim, T. Diemant, R. J. Behm, D. Geiger, U. Kaiser, A. Varzi, S. Passerini, *Adv. Energy Mater.* **2019**, *9*, 1902077.
- [24] M. C. Biesinger, L. W. M. Lau, A. R. Gerson, R. S. C. Smart, *Appl. Surf. Sci.* **2010**, *257*, 887.
- [25] M. C. Biesinger, *Surf. Interface Anal.* **2017**, *49*, 1325.

- [26] K. Yan, Z. D. Lu, H. W. Lee, F. Xiong, P. C. Hsu, Y. Z. Li, J. Zhao, S. Chu, Y. Cui, *Nat. Energy* **2016**, *1*, 16010.
- [27] a) L. Yue, Y. R. Qi, Y. B. Niu, S. J. Bao, M. W. Xu, *Adv. Energy Mater.* **2021**, *11*, 2102497; b) X. Y. Cui, Y. J. Wang, H. D. Wu, X. D. Lin, S. Tang, P. Xu, H. G. Liao, M. S. Zheng, Q. F. Dong, *Adv. Sci.* **2021**, *8*, 2003178.
- [28] Y.-J. Kim, S. H. Kwon, H. Noh, S. Yuk, H. Lee, H. s. Jin, J. Lee, J. G. Zhang, S. G. Lee, H. Guim, H. T. Kim, *Energy Stor. Mater.* **2019**, *19*, 154.
- [29] X. S. Wang, S. W. Wang, H. R. Wang, W. Q. Tu, Y. Zhao, S. Li, Q. Liu, J. R. Wu, Y. Z. Fu, C. P. Han, F. Y. Kang, B. H. Li, *Adv. Mater.* **2021**, 2007945.
- [30] M. Fatahine, D. Guay, L. Roué, *J. Appl. Electrochem.* **2021**, *52*, 149.
- [31] X. B. Cheng, R. Zhang, C. Z. Zhao, Q. Zhang, *Chem. Rev.* **2017**, *117*, 10403.
- [32] D. B. C. Vaalma, M. Weil, S. Passerini, *Nat. Rev. Mater.* **2018**, *3*.
- [33] M. Dahbi, T. Nakano, N. Yabuuchi, S. Fujimura, K. Chihara, K. Kubota, J.-Y. Son, Y.-T. Cui, H. Oji, S. Komaba, *ChemElectroChem* **2016**, *3*, 1856.
- [34] a) R. I. R. Blyth, H. Buqa, F. P. Netzer, M. G. Ramsey, J. O. Besenhard, P. Golob, M. Winter, *Appl. Surf. Sci.* **2000**, *167*, 99; b) X. Liu, M. Zarrabeitia, B. Qin, G. A. Elia, S. Passerini, *ACS Appl. Energy Mater.* **2020**, *12*, 54782.
- [35] G. Homann, L. Stolz, J. Nair, I. C. Laskovic, M. Winter, J. Kasnatscheew, *Sci. Rep.* **2020**, *10*, 4390.
- [36] H. H. Li, H. Zhang, M. Zarrabeitia, H. P. Liang, D. Geiger, U. Kaiser, A. Varzi, S. Passerini, *Adv Sustain Syst* **2022**, 2200109.
- [37] H. Zhang, B. S. Qin, D. Buchholz, S. Passerini, *ACS Appl. Energy Mater.* **2018**, *1*, 6425.